Articles

Interaction of Antagonists with Calmodulin: Insights from Molecular Dynamics Simulations

István Kövesi, Dóra K Menyhárd, Monique Laberge,[†] and Judit Fidy*

Department of Biophysics and Radiation Biology and Research Group for Membrane Biology, Hungarian Academy of Sciences, Faculty of Medicine, Semmelweis University, Budapest, Hungary, and Department of Analytical and Inorganic Chemistry, Budapest University of Technology and Economics, Budapest, Hungary

Received August 1, 2007

We report results of 12 ns, all-atom molecular dynamics simulation (MDS) and Poisson−Boltzmann free energy calculations (PBFE) on calmodulin (CaM) bound to two molecules of trifluoperazine (TFP) and of *N*-(3,3, diphenylpropyl)-*N*′-[1-*R*-(3,4-bis-butoxyphenyl)-ethyl]-propylenediamine (DPD). X-ray data show very similar structures for the two complexes, yet the antagonists significantly differ with respect to their CaM binding affinities, the neutral DPD is much more potent. The goal of the study was to unravel the reason why TFP is less potent although its positive charge should facilitate binding. The electrostatic energy terms in CHARMM and binding free energy terms of the PBFE approach showed TFP a better antagonist, while inspection of hydrophobic contacts supports DPD binding. Detailed inspection of the amino acid contributions of PBFE calculations unravel that steric reasons oppose the favorable binding of TFP. Structural conditions are given for a successful drug design strategy, which may benefit also from charge−charge interactions.

Introduction

CaM[a] is the major calcium receptor inside the eukariotic cells and the major regulator of Ca^{2+}-dependent signaling processes. It is a small acidic protein (16700 Dalton) found in the central nervous system, where it is involved in a variety of cellular functions through the activation of some ∼30 calmodulin-dependent enzymes.[1–6] The available crystallographic data obtained for Ca^{2+}-loaded CaM[7–9] show that its structure is built up from two characteristic "dumbbell"-shaped globular lobes, which are separated by an eight-turn α-helix (residues 67 to 93), connecting the fourth helix of the N-terminal lobe with the first helix of the C-terminal lobe. The central region (residues 75−84) of this long helix forms a linker handle connecting the two domains. Each domain has two "EF−hand" motif Ca^{2+} sites, linked to each other by a short antiparallel β-sheet. The domains have a concave hydrophobic surface in their center surrounded by negative residues. Small angle X-ray scattering data and recent NMR studies have shown that, while the globular domains maintain similar conformations to those observed in the crystal structures, in solution, they are closer to each other by several Ångströms—indicative of a bent central helix under this condition.[10,11] Computer simulations of Ca^{2+}-loaded CaM, show that the central linker[7,12,13] region not only bends, but also converts between a helical and a random coil structure on the ns time scale.[14,15] The flexibility of this central helix largely contributes to the ability of CaM to sample and adopt the numerous versatile conformations required to bind its great diversity of targets with high affinity ($K_d \sim$ nM).[16] It facilitates reorientation of the bulky hydrophobic residues ("hydrophobic patches") located in both the C- and N- domains or that of its IQ motifs, responsible for target recognition.[7,17–19] Several studies have also shown that the conformational change induced by Ca^{2+}-binding exposes the hydrophobic patches of both domains to solvent, thus promoting the binding of CaM to its targets largely driven by the hydrophobic effect.[4,7,20–22]

Of significant biomedical interest is that CaM-induced target enzyme activation can be blocked by several classes of pharmacological effectors: antipsychotics, antidepressants, muscle relaxants, and local anesthetics.[23] CaM thus has been long considered a possible target in drug design strategies.[24] Our goal in this work was to use the tools of molecular dynamics simulation to answer the question what the dominant factors are in suggesting optimal molecular structures for functional antagonists. Can this design be based on understanding the details of possible binding interactions with an antagonist or the dominant factor is the significant conformational change induced by complex formation with any of the bound molecules? For this purpose, we selected to study two structures of biomedical interest, CaM bound to two molecules of trifluoperazine (CaM−TFP) and CaM bound to two molecules of *N*-(3,3,-diphenylpropyl)-*N*′-[1-*R*-(3,4-bis-butoxyphenyl)-ethyl]-propylenediamine (CaM−DPD). Both of these were already studied by X-ray crystallography; actually, the latter antagonist had been designed based on the structure of the binding site in the complex with TFP.[9,25,26]

TFP, a phenothiazine derivative (shown in Figure 1), is one of the most potent antipsychotic agents known and has been the object of several experimental CaM inactivation and binding studies.[27–30] Various investigators have reported dissociation

* To whom correspondence should be addressed. Department of Biophysics and Radiation Biology and MTA Research Group for Membrane Biology, Hungarian Academy of Sciences, Faculty of Medicine, Semmelweis University, Budapest, Puskin utca 9, 1088 Budapest, Hungary. Phone: 36-1-267 6261. Fax: 36-1-266 6656. E-mail: judit@puskin.sote.hu.

[†] Present address: Centre for Structural and Functional Genomics, Department of Biology, Concordia University, 7141 Sherbrooke Ouest, Montréal, QC, H4B 1R6, Canada.

[a] Abbreviations: CaM, calmodulin; DPD, *N*-(3,3,-diphenylpropyl)-*N*′-[1-*R*-(3,4-bis-butoxyphenyl)-ethyl]-propylene-diamine; MDS, molecular dynamics simulation; TFP, trifluoperazine; PBFE, Poisson−Boltzmann free energy.

10.1021/jm701406e CCC: $40.75 © 2008 American Chemical Society
Published on Web 04/15/2008

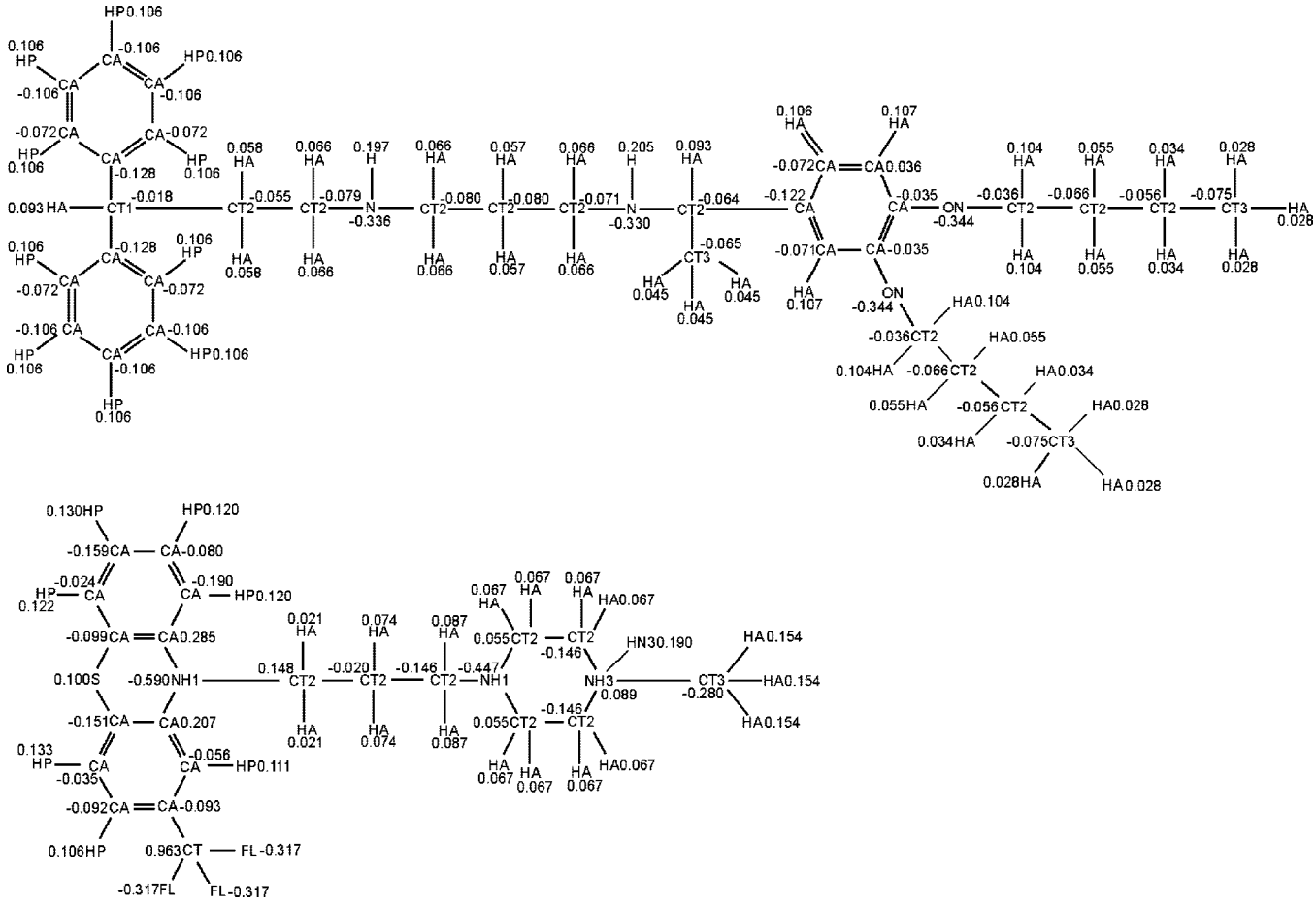

Figure 1. CHARMM atom types and partial charges for newly defined residues: DPD (top) and TFP (bottom).

constants in the 1−8 μM range for the CaM−TFP complex with two,[31] four,[28] and seven[8] TFP molecules bound to CaM. Structures of CaM−TFP have been determined by X-ray crystallography bound to one,[32] two,,[25] and four[33] TFPs. A recent computational study[34] performed on the 1:4 CaM/TFP complex has shed light on the conflicting stoichiometries reported in the literature, supporting the model proposed by Vertessy et al.[25] for only two TFP binding sites. Simulations, although relatively short (2 ns), showed that two of the four TFP molecules dissociate completely from CaM within the first 500 ps, while two TFPs remain bound to the C-domain. This result was in agreement with the C-domain site being the only one occupied in the 1:1 CaM−TFP structure[32] and also being the best-defined site in the 1:4 complex.[33] DPD had been designed to be a better antagonist than TFP.[35] This molecule (Figure 1) belongs to a new arylalkylamine class of CaM antagonists and was recently synthesized as a novel derivative by Chinoin Zrt (Budapest, Hungary). The CaM−DPD structure has also been determined by X-ray crystallography with two DPD molecules bound.[26] DPD was found of much higher affinity for CaM ($K_d \approx 18$ nM)[26] than TFP for binding the first molecule and proved to be more effective antagonist also.

DPD is a quite larger molecule than TFP with more extended hydrophobic regions, while TFP carries a net positive charge that would enable it to interact with acidic residues of the active site. The starting X-ray structures are practically identical for both CaM complexes (superimposed backbone RMSD = 0.62 Å), yet the antagonists have very different binding affinities for binding the first molecules. It is also noteworthy that although negatively charged residues are present and extend into the active site pocket, TFP seems not to make strong and specific contacts with them. The role of electrostatic interactions in forming complexes of CaM and target molecules has been debated.[36] It would be interesting to know why TFP is a less-potent antagonist, while it is capable of both hydrophobic and electrostatic interactions with the binding pocket. It is also a question whether the extended size and hydrophobicity of DPD would be enough to explain its significantly higher affinity for CaM binding. To answer such questions relevant to general drug design strategies, we decided to further refine the structural details of the two selected complexes by relaxing crystal packing constraints in a molecular dynamics simulation (MDS) study and to analyze the significance of relevant interactions in the efficiency of binding an antagonist. We wanted to see whether the contribution of these interactions (derived from knowing the X-ray structure of the complex with antagonists) to the binding free energy[37] would guide our understanding in efficient drug design with respect to calmodulin, where the highly dynamic nature of the conformation plays such an important functional role.

Computational methods are widely used for the characterization of protein effector binding sites, especially now that large amounts of genomic protein structural information are becoming available. In general drug design, common modeling strategies to optimize binding affinity are usually focused on *functional site detection*, that is, on locating binding sites on a protein surface or cleft, followed by considering *functional site similarity*, in which structural/chemical templates are used to classify and locate new binding sites, and finally on *docking*, used to refine and validate functional sites.[38,39] The goal of such studies is, first of all, a quick screening of a variety of compounds, and in most cases, they do not allow for a detailed analysis

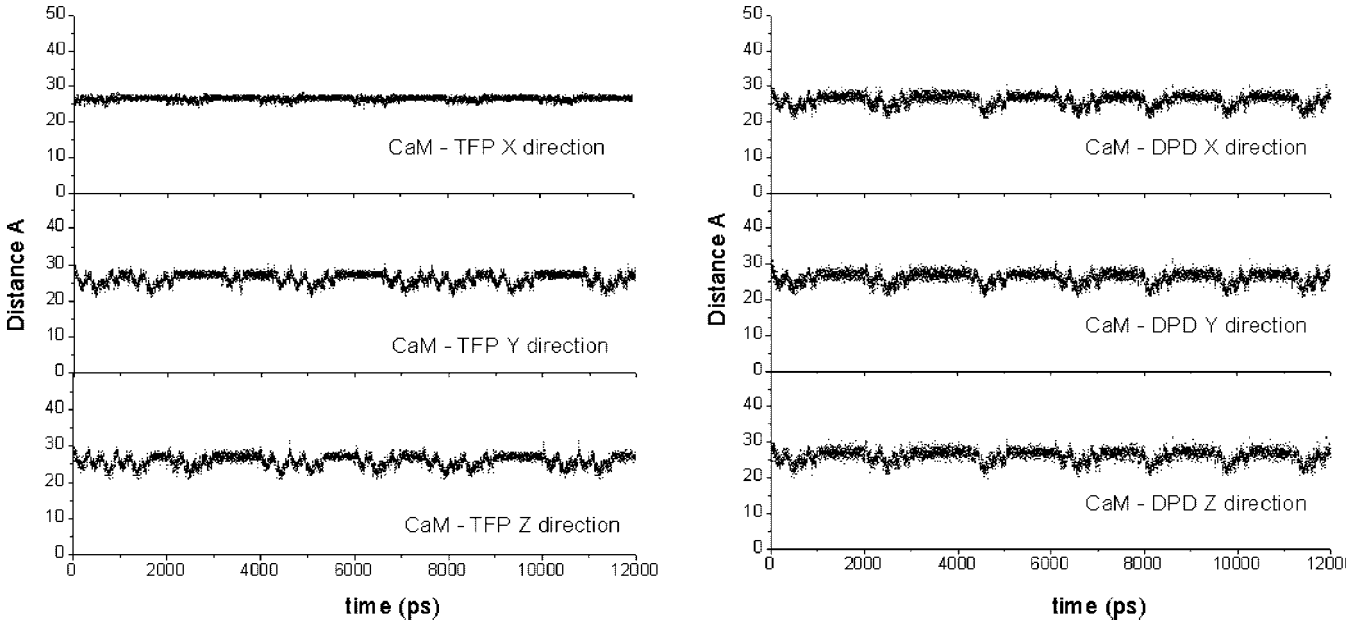

Figure 2. Projection of the least distance between the neighboring proteins in the periodic water-box systems onto the *X*, *Y*, and *Z* axes of both complexes, plotted along the trajectory.

concerning the impact of conformational dynamics on protein-effector recognition processes.[35,40–42] In this study, we performed 12 ns molecular dynamics calculations on fully solvated structures and analyzed the binding interaction terms in the frame of CHARMM and by using a Poisson−Boltzmann free energy approach. No modeling studies have been reported to date on the interaction of CaM with the high-affinity DPD nor on the physiologically relevant 1:2 TFP complex.

Results

Overall Dynamics. Concerning the results of MDS, we found it important to control whether the neighboring protein molecules in the periodic water-box system had an influence on the dynamic motions of each protein. Is it true that the proteins are able to freely adjust their structure to the conditions of motion, temperature, and pressure? For this purpose, we determined the smallest distance between the neighboring protein molecules in the *X*, *Y*, and *Z* directions along the trajectory. These plots are shown in Figure 2 for both studied complexes. It is evident that the molecules can freely move within their water boxes along the trajectory, and the periodic system does not add any constraints to their structure acquired through dynamics. To examine the effect of solvation and dynamics on the structure of the complexes, we calculated the RMSD related to the starting energy-minimized X-ray coordinates after heating and equilibration for the protein backbone and specific regions of interest (C-, N-domain, central helix, antagonists) during the 12 ns simulation time, as shown in Figure 3. The trajectory displays a backbone stability achieved after ∼5 ns, with similar RMSD values for both complexes. The plots for the two domains show rearrangements during the trajectory, which is more significant for the TFP complex. The central helix linker, the flexible helix region that bends to wrap around CaM targets, remains stable, and the RMSD average values are 0.81 Å for DPD and 0.63 Å for TFP. It is interesting to see that the structural change of the two antagonist molecules is different in both cases. In general, the two DPDs show more structural adjustment due to the dynamics.

Figure 4 compares the residue RMSD time-average values of the two complex structures for the last ns. The dynamic

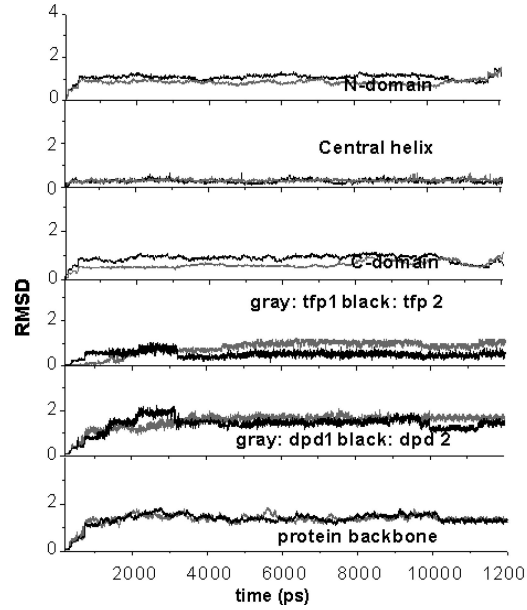

Figure 3. RMSD from the energy-minimized starting structure during the 12 ns trajectories acquired for the CaM−antagonist complexes. Dark trace: CaM−TFP; grey trace: CaM−DPD.

feature of both structures is significantly different; the binding of antagonists seems to affect the mobility of the polypeptide chain in different regions. In the case of the TFP complex, the central helix and its broad neighborhood show significant mobility, while, with DPD bound, the mobility of the linker region seems reduced, except for a single central linker residue (ASP78). Figure 5 compares the RMSF calculated from the trajectory (upper panels) with reference to the energy-minimized structure and the RMSF derived from the experimental B-factors of the C_α-atoms[25,26] using eq 3 (lower panels). The figure shows that the trajectory RMSF ($RMSF_{avg}$ of 1.42 and 2.07 Å for CaM−DPD and CaM−TFP, respectively) values are somewhat larger than those obtained from the X-ray structure refinement procedure ($RMSF_{avg}$ of 1.0 and 1.1 Å for CaM−DPD and CaM−TFP, respectively). Crystallographic refinements always

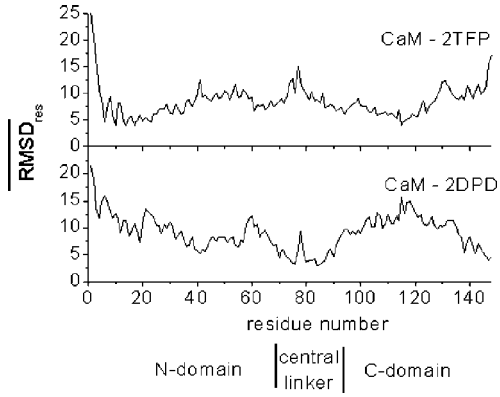

Figure 4. $RMSD_{res}$ values for the main chain of CaM−DPD (top) and CaM−TFP (bottom) complexes.

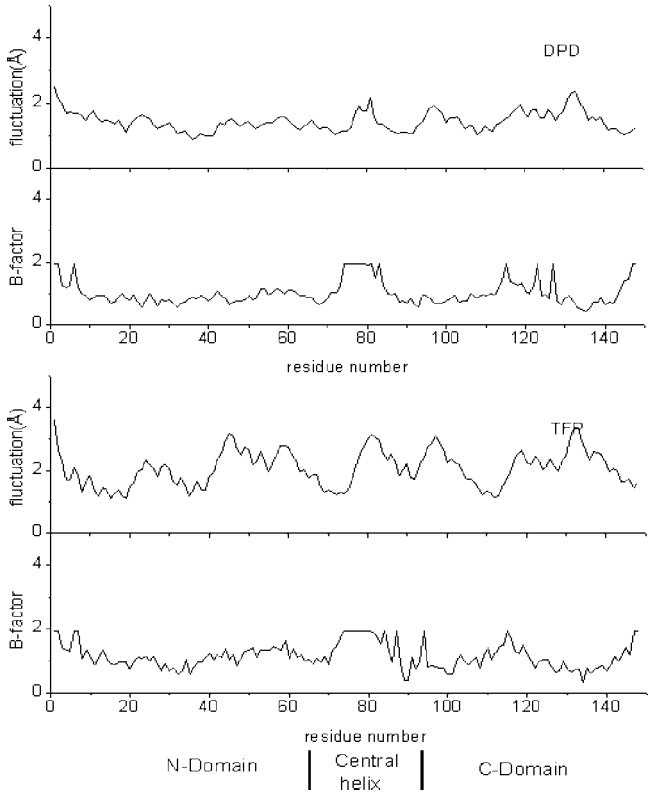

Figure 5. Comparison of RMSF from simulation (upper panels) with the fluctuations derived from experimental crystallographic B-factors (lower panels) for CaM−DPD (top) and CaM−TFP (bottom).

tend to underestimate large fluctuations, and it is accordingly expected to see more pronounced RMSF in solution simulations.[43] An interesting feature of Figure 5 is that the fluctuations show a much more significant mobility in the CaM−TFP complex. These fluctuations seem to affect more or less the whole structure.

In Figure 6, the time evolution of the radius of gyration is shown for both complexes. The R_{gyr} of CaM−TFP remains stable over almost the whole dynamics run, while the R_{gyr} of the DPD complex changes from a higher starting value down to a value still higher than that of the TFP complex. When interpreting the R_{gyr} values, one has to consider that R_{gyr} is a radius in a globular approximation. As discussed below, MDS drives the almost identical starting structures into structures that are distinct also in their overall shape. Thus, R_{gyr} has a different meaning in the two cases.

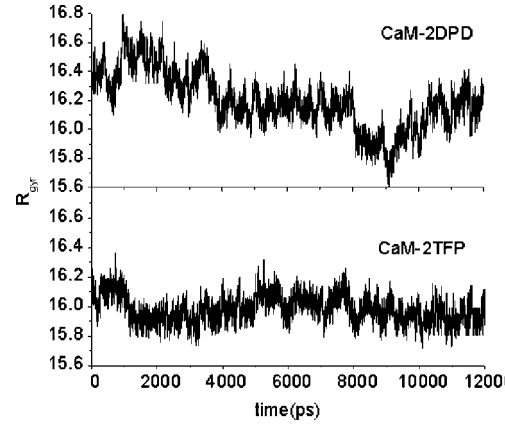

Figure 6. Radius of gyration (R_{gyr}) for all C_α-atoms for the two CaM−antagonist complexes. Black trace: CaM−TFP; grey trace: CaM−DPD.

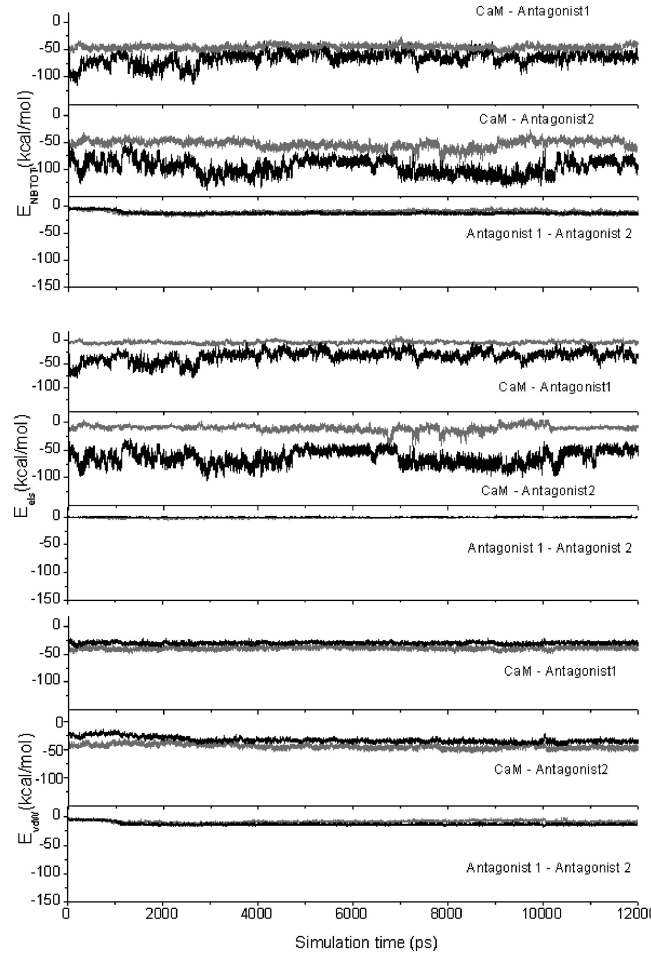

Figure 7. Interaction energies for the CaM−antagonist complexes. Dark trace: CaM−TFP, grey trace: CaM−DPD. Top: total energy; middle: electrostatic, bottom: van der Waals contribution.

In Figure 7, the time-evolution of the interaction energies is plotted for the CaM−antagonist complexes based on the energy terms in CHARMM. The energies are reported separately for each antagonist. Notable differences characterize the respective complexes. In the case of CaM−TFP1, the total energy average is −65.2 kcal/mol and −96.1 kcal/mol for CaM−TFP2. For DPD, the values are −45.4 kcal/mol for CaM−DPD1 and −53.3 kcal/mol for CaM−DPD2. The results suggest that the CHARMM interaction energy is larger when the complex is formed with

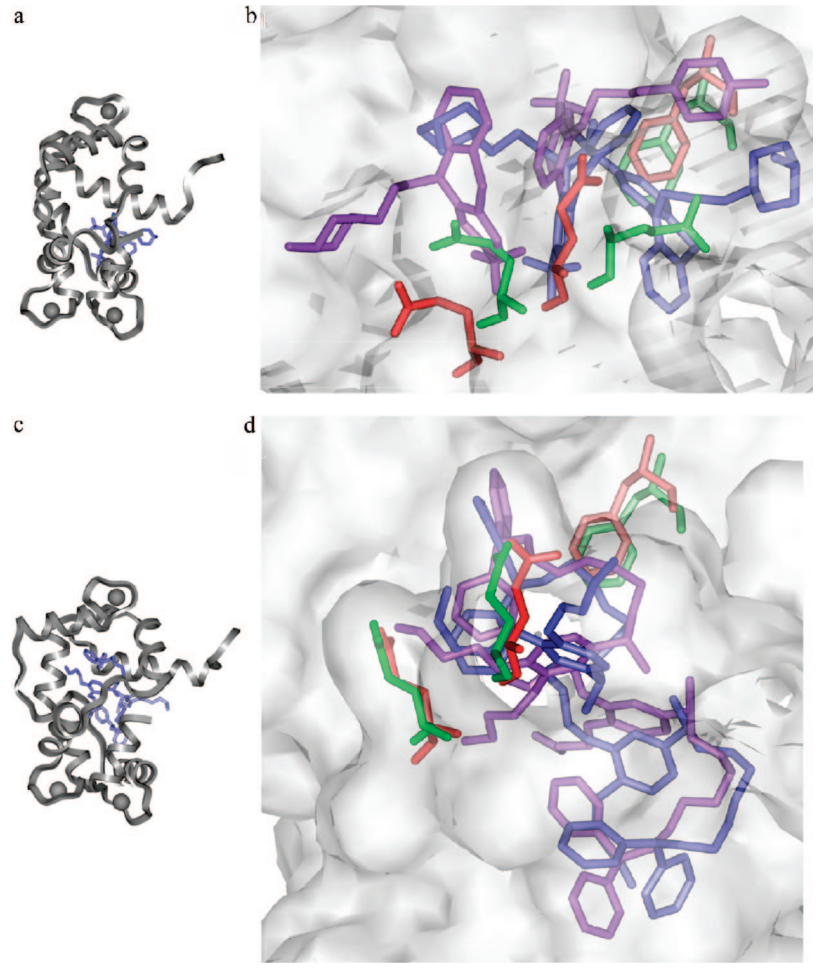

Figure 8. Effect of MDS on the structure of CaM−antagonist complexes. (a) MDS structure (last frame) of the CaM−TFP complex; (b) Structure of the antagonists and interacting amino acids within the CaM−TFP complex in the X-ray structure (violet and red, respectively) and in the MDS structure (blue and green, respectively); (c) MDS structure (last frame) of the CaM−DPD complex; (d) Structure of the antagonists and interacting amino acids within the CaM−DPD complex in the X-ray structure (violet and red, respectively) and in the MDS structure (blue and green, respectively).

TFP. As expected, its major contribution comes from the electrostatic energy term, which is −34.3 kcal/mol for the binding of TFP1 and −63.4 kcal/mol for TFP2, due to the charged piperazine rings. This term is accordingly much smaller for the neutral DPD (−5.5 and −10.5 kcal/mol, respectively). We note, however, that the van der Waals (vdW) term is larger for DPD (−39.5 and −44.1 kcal/mol versus −30.4 and −32.6 kcal/mol of TFP).

The overall structures after MDS (the structures in the figure were determined by overlapping the backbones in a least-squares fitting procedure) and an enlarged view of the position of the antagonists in the X-ray structure and after MDS are shown for both complexes in Figure 8. Comparison of Figure 8a,c shows that the overall shape of the complexes evolved to distinct structures, the complex with TFP is more elongated, while the CaM−DPD complex is more bulky. Figure 8b,d show how the position of the antagonists changed during the dynamics run. There are significant changes for both types of complexes, but the rearrangement is much more dramatic for the two TFP molecules. In this complex, the rearrangement of the interacting amino acids, also shown in the figure, is also significant. This comparison show structural instability of the binding complex in the case of TFP as also indicated by the RMSF data in Figure 5.

Results of the calculations based on HBPLUS to describe the sites of H-bonding and hydrophobic interactions between the protein and the antagonists are shown in Table 1. The residues involved in these interactions are indicated as shaded blocks for the two complexes based on the structures of the last frame in MDS, and of the X-ray data respectively. These data also show that MDS changes the sites of interactions for both kinds of antagonists. The change is more striking in the case of TFP; TFP1 leaves the C-domain during the dynamics and establishes interactions with the N-domain, and TFP2 rearranges itself within the same region of the C-domain. Within the N-domain, Glu11 and Glu14 seem to play an important role in binding. We return to this point when the electrostatic contributions are analyzed.

Electrostatic Calculations. Poisson−Boltzmann free energy calculations have been used in a variety of approximations to describe the energetics of protein complex formation. In the present study, we adapted a procedure that has been used by the Karplus group[44] to calculate and analyze the difference in the binding energy of a charged and a neutral antagonist to a protein matrix. The binding free energy in this approximation was estimated by the electrostatic free energy change accompanying a theoretical "rigid" ligation process, where the conformation of the partners is not allowed to change. In this model, we follow the binding of the antagonists frozen in their structure within the complex into the binding site also frozen in the structure of the complex. Therefore, the greater the conformational rearrangement of complex formation, the less

Table 1. Residues Taking Part in Hydrophobic Interactions and H-Bonds (Grey Boxes) with Antagonists in the X-ray and MDS Structures, as Determined by HBPLUS

	TFP1		TFP2		DPD1		DPD2	
	x-ray	MDS	x-ray	MDS	x-ray	MDS	x-ray	MDS
Glu11								
Phe12								
Glu14								
Ala15								
Phe19								
Ile27								
Leu32								
Val35								
Met36								
Leu39								
Gln41								
Met51								
Val55								
Phe68								
Met71								
Met72								
Met76								
Val91								
Phe92								
Ile100								
Leu105								
Met109								
Leu116								
Met123								
Met124								
Ile125								
Glu127								
Ala128								
Val136								
Phe141								
Met144								
Met145								

Table 2. ΔG (in kJ/mol) of Direct Interaction (dir), Ligand Desolvation (ligdes), and Protein Desolvation (protdes) of Ligand and Protein, Respectively, Based on the Structures of X-ray Crystallography and of MDS

	X-ray structures						MDS derived structures					
	TFP complex			DPD complex			TFP complex			DPD complex		
	$\epsilon = 2$	$\epsilon = 4$	$\epsilon = 10$	$\epsilon = 2$	$\epsilon = 4$	$\epsilon = 10$	$\epsilon = 2$	$\epsilon = 4$	$\epsilon = 10$	$\epsilon = 2$	$\epsilon = 4$	$\epsilon = 10$
ΔG_{dir} (kJ/mol)	−104.4	−69.9	−46.6	−10.5	−6.4	−3.7	−58.6	−46.8	−37.6	−2.0	−1.0	−0.4
ΔG_{ligdes} (kJ/mol)	59.8	30.0	11.8	47.8	22.3	7.4	52.6	27.0	11.2	41.2	19.6	6.7
$\Delta G_{protdes}$ (kJ/mol)	180.8	90.6	35.4	78.4	40.2	16.5	99.3	49.6	19.5	53.3	26.1	9.9
ΔG_{tot} (kJ/mol)	136.2	50.7	0.6	115.6	56.2	20.2	93.4	29.9	−7.0	92.6	44.7	16.2

adequate this model is with respect to the real binding process. In the case of CaM, as it is well-known, the change from its dumpbell shape without antagonists to the globular, compact structure of the complex forms clearly means a significant conformational change. Obviously, this cannot be declared negligible, but one has to note that there is no experimental data for the structure without ligand. Most probably, CaM without antagonist in a physiological solvent cannot even be characterized by a single, well-defined structure, supposing a distribution of structures would be more realistic.[12–15] The basis for using the rigid model in the present study was that the significant conformational change upon binding the antagonists can be supposed similarly characteristic for both of the compared complex formations. Thus, we would neglect similar terms for both structures in the comparison.

The calculations were performed by using the X-ray data and also those of the last frame in MDS, which we found well representing the average structure for the last 2 ns of the trajectory (data not shown). Table 2 shows the electrostatic binding free energy terms and total free energy values for the compared systems. In Figure 9a,b we plotted the energy contributions for all residues on the same scale as obtained for the X-ray data and for the MDS structure at $\epsilon = 4$, respectively. As seen in Table 2, using any of the three inner dielectric values, MDS brought significant improvement in the electrostatic binding free energy of the CaM−2TFP complex. As it can be expected, and seen both in the table and in the figures, the TFP ligand well outperformed the uncharged DPD in its direct charge−charge interaction with the protein, both in the X-ray and in the MDS-derived structures. However, due to the coupled, formidable protein desolvation terms, at the low inner dielectric value of 2, DPD proved to be the favored ligand and, even at higher inner dielectric values, desolvation terms level out the favorable direct interactions of the TFP ligands. In Table 3 we show the data for significant energy contributions at the two higher ϵ values, corresponding also to those plotted in Figure 9a,b for $\epsilon = 4$. Some important structural details at the sites of interactions for the two TFP molecules in the MDS structure are visualized in Figure 10. One can see that the carboxylate oxygens of Glu11 and Glu14 of CaM all reach close to the positive pyridino-N of TFP1 and TFP2, respectively (with an average distance of 4.8 Å), as also indicated by the data shown in Table 1. One has to realize, however, that the polarized methyl group attached to the same N of TFP (at an average distance of 3.7 Å from the glutamate oxygen) opposes a direct, clear charge−charge interaction with the N. This effect is pinpointed as a great protein desolvation energy showing that the interaction of the Glu residues would be more favorable with water. The

Table 3. ΔG (in kJ/mol) of Direct Interaction (dir) Protein Desolvation (protdes), and the Total Electrostatic Free Energy (tot) of the Dominating Interactions of the X-ray- and MDS-Derived Structures, Determined at Different ϵ Values

CaM−TFP

	X-ray structures						MDS-derived structures					
	ΔG_{dir}		$\Delta G_{protdes}$		ΔG_{tot}		ΔG_{dir}		$\Delta G_{protdes}$		$\Delta G_{tot>}$	
	$\epsilon = 4$	$\epsilon = 10$	$\epsilon = 4$	$\epsilon = 10$	$\epsilon = 4$	$\epsilon = 10$	$\epsilon = 4$	$\epsilon = 10$	$\epsilon = 4$	$\epsilon = 10$	$\epsilon = 4$	$\epsilon = 10$
Glu11	−3.3	−2.7	7.3	3.4	4.0	0.7	−7.6	−5.2	17.9	7.1	10.3	1.9
Glu14	−4.1	−2.8	9.0	3.9	4.8	1.1	−2.6	−2.5	5.7	2.3	3.2	−0.2
Glu114	−7.4	−4.2	25.9	9.4	18.4	5.2	−0.6	−0.6	0.1	0.1	−0.5	−0.5
Glu120	−8.8	−5.3	16.0	5.9	7.2	0.6	−2.7	−2.0	1.1	0.4	−1.6	−1.6
Glu123	−1.7	−1.3	2.9	1.3	1.2	0.0	−2.8	−2.5	2.3	1.2	−0.5	−1.3
Met124	−1.6	−0.7	3.2	1.1	1.6	0.4	−0.9	−0.4	2.0	0.7	1.1	0.3
Glu127	−3.6	−2.9	18.2	7.3	14.6	4.4	−2.5	−2.5	5.4	2.3	2.9	−0.2

CaM−DPD

	X-ray structure $\Delta G_{protdes}$		MDS-derived structure $\Delta G_{protdes}$	
	$\epsilon = 4$	$\epsilon = 10$	$\epsilon = 4$	$\epsilon = 10$
Glu11	4.4	2.1	1.2	0.6
Glu14	4.1	1.8	1.3	0.7
Met71	3.3	1.0	1.0	0.4
Glu84	1.6	0.7	0.1	0.1
Glu87	2.2	0.9	0.0	0.0
Met124	2.2	0.8	0.2	0.1

carboxyl oxygens of Glu120 (could not be shown in Figure 10) attracted to the positive moiety of TFP2 come into close contact with the apolar Met124 side chain, which is again unfavorable. Thus, in the TFP structures, direct interaction that would promote binding is always overpowered by even greater and unfavorable desolvation.

The fitting of the two TFP molecules into the protein remains problematic in both approaches. As visualized in Figure 9 ($\epsilon = 4$), the most critical charge−charge direct interaction terms change from Glu11, Glu14, Glu114, Glu120, Glu123, Glu127 in the X-ray structure to Glu11, Glu14, Glu127 after MDS. The magnitude of the contributions also change; the fitting becomes better after MDS, but the shortcoming of the TFP complex remains basically the same, where the TFP-s cannot reach close enough to optimize the overall effect. Concerning the X-ray crystallography data of the TFP complex (1A29.pdb), it has been reported that Glu120, forms an H-bond with TFP1 (25). However, in a solvated system, Glu120 is not embedded in the hydrophobic interior of CaM, rather it reaches into the solvent and according to the results in a fully solvated state, will more readily interact with water molecules than with the bulky, partly hydrophobic TFP as a H-bond donor.

As it was mentioned above, the energy terms in Table 2 show the improvement of the structure along with MDS in the case of the CaM−2DPD complex as well. The direct interaction term became less favorable at all inner dielectric values, however, a considerable improvement was achieved by the protein desolvation terms. The overall effect was an optimization of the electrostatic binding free energy of the complex. Interestingly, the desolvation energy was made more favorable by the better desolvation of polar resides, those of Glu11, Glu14, Glu84, and Glu87 (and two methionines, Met71 and Met124), which are allowed by the MDS-derived arrangement to maximize their solvent contacts. These energy contributions are shown in Figure 9 and Table 3. In case of interaction with these charged residues, the hydrophobic nature of DPD promotes their turning to the surface of the protein instead of the interior, not interfering with their solvation is a beneficial effect of the ligand.

Desolvation energy thus plays a major role in defining the electrostatic fit of the complexes studied by us. The PBFE approach, however, can not directly account for the role of the hydrophobic effect. To obtain an estimation concerning the role of hydrophobic interactions, we determined the SASA values of those amino acids that may be involved in the interactions with the antagonists for two cases: when the antagonist is present (SASA1) and when it is omitted from the structure (SASA2). After subtracting the two values, the ΔSASA = SASA2 − SASA1 data, characteristic for the effect of binding the antagonist, are given in Table 4. In the list of the amino acids, we considered the values for the hydrophobic residues for both complexes and for both kinds of structures. High ΔSASA values report significant hydrophobic effects. The conclusion from the comparison of X-ray and MDS structures is that for the DPD complex, MDS increased the role of hydrophobic interactions, while for TFP these contacts became weaker. As it is expected in a comparison of the two antagonists, and was also indicated by the results shown in Table 1, the ΔSASA values show that the hydrophobic contacts are very significant in the DPD complex in both kinds of structures, while these contacts are rare in the complexes with TFP.

Discussion

Our purpose with this study was to investigate the structure of two CaM−antagonist complexes of very much different dissociation constants after relaxing the starting X-ray structure in solvent by involving molecular dynamics to yield better insights in the binding specificity of CaM to antagonists, and may be to target proteins and peptides, at the molecular level. The respective X-ray structures of both complexes showed[25,26] virtually identical protein folds for both structures. Our working hypothesis was that there could be an important contribution from protein dynamics in forming the stable structure of the complexes, and we believe that our results warrant this viewpoint. The notion that antagonists bound within the calmodulin active site possess freedom of movement and that even domain movements can be expected, could also be predicted from experimental findings.[7,12,13] In X-ray crystallography, the three crystal structures describing the calmodulin−

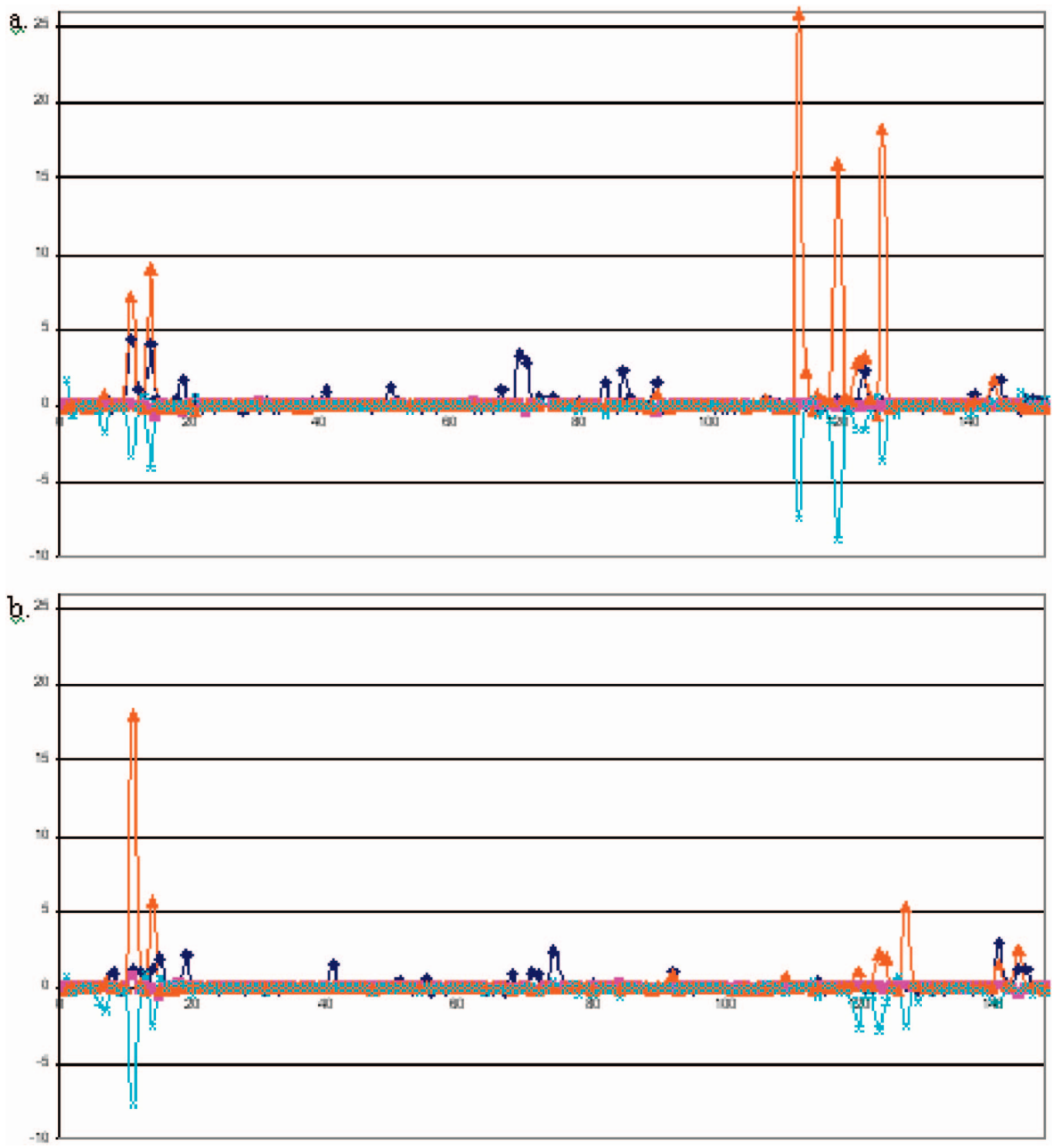

Figure 9. (a) ΔG (in kJ/mol) of direct interaction (purple in CaM−2DPD and light blue in CaM−2TFP) and protein desolvation (dark blue in CaM−2DPD and orange in CaM−2TFP) for each residue of the CaM−2TFP and CaM−2DPD complexes in their X-ray-derived conformations. (b) Same for the MDS-derived states.

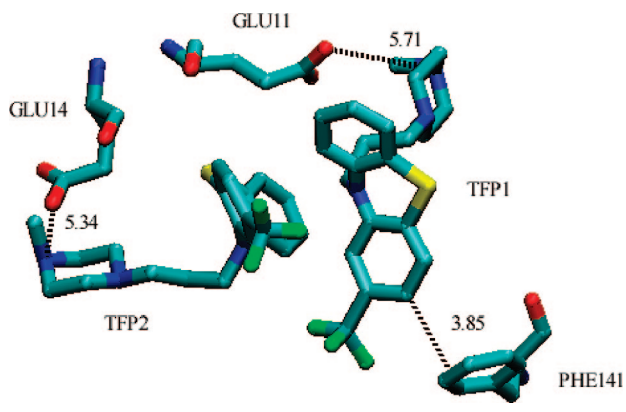

Figure 10. The two TFP molecules at the binding site after MDS.

TFP complex of different stochiometries (1:1, 1:2, and 1:4) and one of the two calmodulin−DPD complex structures were all determined from crystals of the same space group. Thus, in all cases, the crystal constraints were identical. Still, if one looks at the CaM−TFP complexes, the position of the antagonist molecules may differ. Even though TFP1 of the 1:2 and 1:4 complexes binds at overlapping sites, this is not the case for the 1:1 complex. Additionally, TFP2 of the 1:4 complex becomes shifted over 9 Å from the position it occupies in the 1:2 complex (a position that remains unoccupied in the 1:4 complex). This is of functional significance also because the former is a C-domain binding site while the latter is at interdomain location. In the case of the DPD complex, the power of symmetry restraints was also nicely demonstrated. In the data bank, one can find two structures for the CaM−DPD complex, determined from crystals belonging to a different space group.

Table 4. SASA Difference Created by Binding of the Ligand in the Case of the X-ray- and MDS-Derived Structures of the CaM−2TFP and CaM−2DPD Complexes

	ΔSASA			
	DPD		TFP	
	X-ray	MDS	X-ray	MDS
Gln8	0	1.1	0	0
Glu11	6.2	11.6	18.7	47.8
Phe12	***0***	***14.1***	***0***	***0***
Glu14	5.8	5.0	29.8	33.9
Ala15	***29.1***	***22.0***	***11.3***	***25.5***
Leu18	***26.6***	***12.7***	***39.1***	***22.5***
Phe19	***44.9***	***61.6***	***0***	***15.2***
Ile27	***13.1***	***20.2***	***10.4***	***0***
Leu32	***23.3***	***46.7***	***6.5***	***13.2***
Val35	***15.9***	***17.5***	***13.0***	***0***
Met36	15.8	18.6	0	0
Leu39	***7.4***	***34.7***	***0***	***0***
Gln41	17.5	4.1	0	0
Met51	15.8	17.8	0	0
Ile52	***10.6***	***12.3***	***0***	***0***
Val55	***12.6***	***23.2***	***0***	***0***
Ile63	***11.6***	***29.6***	***0***	***0***
Phe68	***17.0***	***26.0***	***0***	***0***
Met71	36.8	38.7	0	0
Met72	55.2	58.1	0	0
Lys75	0	7.4	0	0
Met76	18.2	23.3	0	0
Glu84	5.7	0	0	0
Phe91	***19.8***	***0***	***0***	***0***
Phe92	***43.1***	***31.1***	***14.5***	***18.4***
lle100	***16.4***	***15.8***	***19.7***	***0***
Leu105	***20.2***	***21.0***	***19.3***	***0***
Val108	***6.0***	***12.3***	***0***	***0***
Met109	28.7	24.2	28.6	14.0
Leu112	***16.4***	***11.4***	***1.1***	***0***
Glu114	0	0	25.5	0
Leu116	***1.0***	***1.1***	***18.8***	***13.0***
Glu120	0	0	26.0	15.4
Val121	***0***	***0***	***0***	***0***
Met124	0	0	69.7	36.2
Ile125	***17.7***	***9.1***	***17.8***	***0***
Glu127	0	0	25.3	32.0
Ala128	***6.6***	***8.7***	***18.6***	***15.7***
Val136	***0***	***13.4***	***17.1***	***11.1***
Phe141	***14.3***	***17.0***	***29.2***	***10.5***
Met144	36.6	19.2	36.5	54.6
Met145	54.7	47.9	0	0

These structures contained DPD in a reoriented conformation and evidence for considerable domain displacement was also detected.[26]

The present 12 ns of simulations proved adequate to equilibrate the two CaM complexes and to unravel important differences between "static" and "dynamic" models. Inspection of Figure 8 and results of the simulation clearly show that the models equilibrated after MD simulations present marked structural differences between the two complexes, with a backbone RMSD of 3.5 Å between the two simulated models as opposed to an insignificant RMSD of 0.6 Å for the X-ray structures. The resulting DPD complex clearly adopts a distinctly more globular conformation, similar to that of target-bound CaM.[20] The net result of this globular structure (as opposed to the more elongated CaM−TFP structure) is to better position the DPDs via favorable hydrophobic contacts. Table 1 shows that the contacts in several cases are not the same as those in the X-ray structure. In this table, interactions with atomic distances characteristic for H-bonding and hydrophobic interactions are labeled. For the two DPD molecules, altogether 16 contacts are indicated, while for the TFP molecules only 3 and 2 contacts were found, respectively. The significance of hydrophobic interactions in the case of DPD binding is also demonstrated by the ΔSASA data in Table 4. Hence, we confirm the finding that one reason for DPD being the more efficient antagonist is that it is optimally wrapped by the protein. Extensive contacts with the CaM hydrophobic patches not only enhance affinity but also prevent target binding because the binding sites of both domains are occupied. Additionally, DPD maintains the interactions with central helix residues (Met76, Phe92) during the simulation, thus anchoring the helix to reduce its flexibility and prevent antagonist escape. In marked contrast, TFP has hydrophobic contacts only with a few residues.

To study the role of electrostatic interactions in complex formation, we used a very rough approximation, a "rigid binding" approach to determine the energetics of antagonist binding by PBFE calculations. MDS lowered the electrostatic binding free energies for both complexes independently from the inner dielectric value used, thus providing further support for the validity of the MDS derived structures. At the low inner dielectric value of 2, the DPD complex is favored in both the X-ray- and MDS-derived arrangements, but at the more realistic values of 4 and especially of 10, TFP becomes the better ligand of the two, therefore, PBFE results alone do not allow clear distinction of them. However, analysis of the details did provide important insights into how it is possible that CaM, with negatively charged amino acids at the binding site, can establish both specific and nonspecific bonds with its targets based on electrostatic interactions.[36]

PBFE calculations are not particularly sensitive to hydrophobic effects, hydrophobicity is introduced through the desolvation terms. Desolvation energy, although not an explicit hydrophobic measure, does describe how well the residues accept the replacement of binding site solvent molecules by an uncharged, ligand-shaped and -sized, low dielectric medium; in other words, how the residues tolerate loss of their solvent contacts upon complexation. Desolvation free energy of the hydrophobic residues in the two CaM complexes studied by us is quite similar both in the X-ray structures and in the MD-derived state, due to the fact that hydrophobic contacts not met by the ligand are usually fulfilled by the hydrophobic patch of the other CaM lobe; therefore, the change in going from the closed and solvated form to the closed and ligand bound form is, for most hydrophobic groups, not notable. Interestingly, in this case, the considerable difference that was seen between the desolvation free energy of the DPD and TFP complexes, greatly favoring the DPD ligand, arises from those polar residues of the binding site that TFP attempts to approach, attracted by their negative charge. TFP shields these polar segments from interaction with the solvent−water molecules, thus creating a large and unfavorable desolvation term, while it cannot reach close enough to compensate this effect by the accompanying charge−charge interaction. This is also reflected in the high values of solvent accessible surface area differences given for the major electrostatic partners of TFP (Glu11, Glu14, Glu127) in Table 4, compared to those of the DPD complex, especially in the MD-derived structure.

Looking at the structural features behind the energy data, we have to note that the negatively charged amino acids of the CaM active site are surrounded by hydrophobic residues; for example, along Glu11, we find Phe12, by Glu14, Ala15 and Leu18 and the through-space neighbor of Glu120 is Leu116. It seems that the positively charged moieties of the TFPs are not able to reach close enough to the negative charge centers to make up for their accompanying loss of water contact because of the surrounding, often bulky, hydrophobic groups. From the TFP side of the

contact, it may also be unfortunate that the positive charge of its pyridino-N not only may polarize the neighboring methyl group, but in interaction with all neighboring electron clouds may just be part of an extended dipole type of charge distribution instead of being a point−charge partner in the interaction with the amino acids. That the Glu and Asp residues of CaM are indeed difficult to reach, can be demonstrated by analyzing the available structural data for the peptide complexes of the protein.[26,45–58] We identified 53 H-bond contacts between negatively charged amino acids of CaM and its complexed peptides. In 85% of the cases, the interacting partner was a Lys or an Arg residue, and in only eight cases did other possible proton donors, such as Thr, His, Ser, Asn, and Gln, take part in the interactions. In the 13 complexes analyzed, in no cases did the carboxylate oxygens of CaM associate with backbone amide nitrogens of the target peptide. This demonstrates nicely that the negative charge centers of CaM prefer interacting with such molecular segments where an isolated positive charge is located at the end of a long, flexible aliphatic chain. We suggest that, in such cases, the interaction of CaM and target (antagonist) can be well-defined and specific. TFP is not such a case: the positive charge is carried by the N of the piperazine ring and the neighboring methyl group. We propose that the binding of TFP represents a case of nonspecific interactions with respect to CaM, that is, when the binding partner can not really benefit from its positive charges due to steric constraints.

The conclusions of this study are strongly related to a successful drug design strategy for the CaM−antagonist approach. Our opinion is that a well-designed molecule should not only maximize hydrophobic contacts, but its binding may be promoted also by direct charge−charge contacts, in case it carries positive charge in a proper configuration. The charge should be located at the end of a flexible arm, so that the structure could benefit from electrostatic contacts, without interfering with the proper solvation of polar residues lining the ligand entrance region of the protein.

Computational Methods

Molecular Dynamics. Molecular dynamics simulations were performed using CHARMM,[59] version c32b1, with the CHARMM22 all-atom parameter set and the TIP3P water potential[60] and NAMD[61] to extend the production runs in the ns-time scale. Initial coordinates for the two CaM complexes were obtained from the RCSB data bank, namely, CaM with 2 DPD molecules (1QIV.pdb, 2.64 Å resolution)[26] and CaM with 2 TFP (1A29.pdb, 2.74 Å resolution).[25] Missing residues (Ala1, Asp2, Ala147, and Lys148) were added with the *biopolymer* module of the *InsightII* software package (Accelrys, San Diego). The antagonist molecules were parametrized for CHARMM following available protocols.[62,63] For this purpose, all quantum chemical computations and normal mode calculations were performed using the NWCHEM package[64,65] with full geometry optimizations of the antagonist structures performed using DFT[66–68] with the B3LYP functional[69] and the SBKJC/VDZ EPC.[70] Partial atomic charges were derived by using the CHELPG protocol.[71] Parameter refinement for CHARMM was then performed using AFMM[72] (Figure 1 and Table 5). The models of both complexes were further prepared for simulation by addition of explicit hydrogens using HBUILD, as implemented in CHARMM, and consistent with pH 7.0. Both complexes were first gently minimized in vacuo using a conjugate gradient algorithn with harmonic constraints imposed on backbone atoms decreased as follows: 150, 100, 50, 20 kcal/mol/Å^2. To achieve charge neutrality, counterions were added using *Solvate 1.0*,[73] which places Na^+ and Cl^- counterions at physiological concentration (0.154 mol/L) according to a Debye−Hückel distribution, followed by a large number of (2000000) of Monte Carlo equilibration steps. For CaM−TFP, 26 Na^+ ions were added and 11 Cl^-, while 28 Na^+ and 12 Cl^- were required for CaM−DPD. The complexes and counterions were then placed into truncated octahedral cells filled with TIP3P water molecules. The size of the cells were 67 × 76 × 74 Å for CaM−DPD, and 70 × 67 × 63 Å for CaM−TFP. Waters overlapping the protein or counterions were deleted, and the final simulation systems consisted of 39654 atoms for CaM−DPD and 31389 atoms for CaM−TFP. The solvated models were then subjected to energy minimization. With the proteins fixed, 200 steps of steepest descent minimization were first applied to relax solvent and counterions. A second minimization was then performed on the whole system with gradually decreasing backbone harmonic force constants, as described above. NPT molecular dynamics were

Table 5. CHARMM Atom Types and Parameters for DPD and TFP

TFP

bond	K_r kcal/(mol Å^2)	r_{eq} (Å)
CA- NH1	390.000	1.222
CA-S	230.000	1.773

angle	K_θ kcal/(mol rad^2)	q_{eq} (deg)
CA-CA-NH1	65.000	120.000
CA-CA-S	65.000	120.000
CA-CT-FL	60.000	109.470
CA-NH1-CA	35.000	109.470
CA-S-CA	75.000	98.000

torsion	periodicity	V kcal/(mol rad^2)	γ (deg)
CA-CA-NH1-CA	3	0.600	0.000
CA-CA-NH1-CT2	4	0.670	0.000
CA-CA-S-CA	3	0.400	0.000
CA-NH1-CT2-CT2	3	0.067	0.000
CA-NH1-CT2-HA	3	0.067	0.000
CT2-CT2-NH1-CT2	3	1.440	0.000
CT2-CT2-NH1-CT3	3	1.440	0.000
HA-CT2-NH1-CT2	3	1.440	0.000
HA-CT2-NH1-CT2	3	1.440	0.000
HA-CT3-NH1-CT2	3	1.440	0.000

improper	periodicity	V(dihe) (kcal/mol)	γ (deg)
CA-CA-CA-NH1	2	68.560	180.000
CA-CA-CA-S	2	56.090	180.000

DPD

atom type	atom mass	description
ON	16.000	etheroxygen

bond	K_r kcal/(mol Å^2)	r_{eq} (Å)
ON-CT2	87.996	1.430
ON-CA	86.617	1.380

angle	K_q kcal/(mol rad^2)	θ_{eq} (deg)
CT2-ON-CA	52.560	110.690
CA-CA-ON	48.820	119.220
CT2-CT2-ON	47.760	125.400
HA-CA-ON	45.200	120.000
HA-CT2-ON	42.110	108.160

torsion	periodicity	V kcal/(mol rad^2)	γ (deg)
CA-CA-CA-ON	4	3.168	0.000
HA-CA-CA-ON	4	0.158	0.000
CA-ON-CT2-HA	4	0.305	0.000
CA-ON-CT2-CT2	2	0.305	0.000
CA-CA-ON-CT2	4	0.997	0.000
ON-CA-CA-ON	1	3.168	0.000

atom type	vdW radius (Å)	ϵ (kcal/mol)
ON	1.700	−0.120

performed under periodic boundary conditions and initiated with 30000 steps of heating to 300 K, followed by 50000 steps of equilibration and subsequent acquisition of 12 ns production trajectories. The dielectric constant was set to 1.0. All hydrogen bonds were constrained using the SHAKE algorithm,[74] and an integration time step of 1 fs was used. Coordinates were saved every 10 ps, and the nonbonded lists were updated heuristically. Full electrostatics were calculated using the particle mesh Ewald[75] method, with a grid spacing less than 1 Å and a κ value of 0.34 $Å^{-1}$.[76] The cutoff distance was 12.0 Å, and the switch distance was 10 Å. Constant temperature (300 K) was controlled with the Langevin method, and constant pressure (1.01325 bar) was maintained using the Langevin piston method.[77] Data analysis was performed on the production run of the acquired trajectories for both complexes. Interaction energies were calculated using available CHARMM protocols. Hydrogen bonding patterns and hydrophobic interactions were determined using HBPLUS, version 3.0,[78] a program developed to calculate H-bonds.[78] This program identifies bonding patterns between an effector and a protein based on the atomic distances, angles, and atom types and HBPLUS input. HBPLUS selects donor and acceptor atoms and computes all the H-bonds that satisfy selected geometric criteria. Cutoff distances for H-bonding and donor−acceptor distances were 2.7 and 3.3 Å, respectively; the donor−H−acceptor angle was set at any angle greater than 90°.

Trajectory Analysis. The average structures of the CaM complexes $\langle x_i \rangle$ obtained from the last ns of the 12 ns trajectories were calculated as

$$\langle x_i \rangle = \frac{1}{N}\sum_{k=1}^{N} x_i(t) \tag{1}$$

over the values of each atomic Cartesian coordinate x_i at different times t during the length of the production trajectory.

The root-mean-square deviations of the C_α atoms in the trajectories and the radius of gyration of the proteins, R_{gyr}, were monitored as a function of time with respect to the starting structures after solvation and energy minimization. The root-mean-square deviation is defined as

$$\mathrm{RMSD} = \left(\frac{1}{N_{C\alpha}}\sum_{i=1}^{N_{C\alpha}} (r_i^{A}(t) - r_i^{B})^2\right)^{1/2} \tag{2}$$

where A and B refer to the two structures being compared, N is the number of C_α atoms. Structure B is the reference structure after energy minimization. The difference is taken after a least-squares fit superposition. RMSD time averages for the last ns were calculated for the amino acid residues and denoted by RMSD_{res} The average of atomic fluctuations was calculated from the simulations and compared to the experimental B-factors of the starting X-ray structures by the relation[79]

$$\mathrm{RMSF} = \langle \Delta r_i^2 \rangle^{1/2} = (3B_i/(8\pi^2))^{1/2} \tag{3}$$

where Δr_i is the atomic displacement of atom i from its average position. The bracket refers to the time average of fluctuations for each residue for the time course selected as the last ns of the simulations. The nonresolved residues in the crystallographic B-factors with values of 0 were set to 100 $Å^2$, which corresponds to a RMSF of 2 Å.[80]

The radius of gyration is defined as

$$R_{gyr}(t) = \left(\frac{1}{N_{C\alpha}}\sum_{i=1}^{N_{C\alpha}} (r_i(t) - r_{CG}(t))^2\right)^{1/2} \tag{4}$$

where $r_i(t)$ and $r_{CG}(t)$ are the coordinates of atom i and of the center of gravity of the protein, respectively, at time t, with $N_{C\alpha}$ representing the total number of C_α atoms involved.

Electrostatic Free Energy Calculations. Electrostatic free energy of binding was calculated by subtracting the electrostatic free energy of the solvated protein and of the antagonist molecules from the electrostatic free energy of the solvated structure of the complex formed with each of the two antagonists.

$$\Delta G_{bind} = G_{PL} - G_P - G_L \tag{5}$$

We started from the following approximation: we left the conformation of the separated protein and the two antagonists unchanged relative to that in the complex. In this way, the significant conformational change upon binding the antagonists, especially the first one, was not taken into consideration. The validity of this approach will be discussed later in details. Briefly, since our goal was to compare the ΔG_{bind} values for two complexes, we may have supposed that in the $\Delta\Delta G_{bind}$ value, the contribution of the neglected terms would practically cancel each other.

The electrostatic free energy of binding defined as described above was, in turn, broken into three components of physical meaning, according to the procedure described by M. Karplus and co-workers[44] as follows:

$$\Delta G_{bind} = \Delta G_{dir} + \Delta G_{des}^{PL-P} + \Delta G_{des}^{PL-L} \tag{6}$$

where ΔG_{dir} is the *direct interaction* term, describing the interaction of atomic point charges of one of the components exposed to the electrostatic potential of the other part, while the ΔG_{des} is the *desolvation* energy (protein and antagonist desolvation, corresponding to the second and third term of eq 6, respectively), which in our assumption represents the change in protein−solvent interactions and antagonist−solvent interactions upon complex formation. These terms can be calculated as follows:

$$\Delta G_{dir} = \frac{1}{2}\sum_{\substack{i\in \mathrm{prot}\\ j\in \mathrm{lig}}} q_i V_{j\to i}^{PL} + \frac{1}{2}\sum_{\substack{i\in \mathrm{prot}\\ j\in \mathrm{lig}}} q_j V_{i\to j}^{PL} \tag{7}$$

where q_i and q_j are partial charges of protein and ligand atoms, $V_{j\to i}^{PL}$ denotes the electrostatic potential produced by the partial charge of ligand atom j at atom i of the protein in the complex, while $V_{i\to j}^{PL}$ denotes the potential at atom j of the ligand resulting from the partial charge of the protein atom i. The protein desolvation term has the form

$$\Delta G_{des}^{PL-P} = \frac{1}{2}\sum_{\substack{i\in \mathrm{prot}\\ j\in \mathrm{prot}}} q_i\left(V_{j\to i}^{PL} - V_{j\to i}^{P}\right) \tag{8}$$

where $V_{j\to i}^{PL}$ is the electrostatic potential at atom i of the separately solvated protein resulting from the partial charge of another protein atom j. The antagonist desolvation term is calculated by:

$$\Delta G_{des}^{PL-L} = \frac{1}{2}\sum_{\substack{i\in \mathrm{lig}\\ j\in \mathrm{lig}}} q_i\left(V_{j\to i}^{PL} - V_{j\to i}^{L}\right) \tag{9}$$

where $V_{j\to i}^{L}$ is the electrostatic potential at atom i of the separately solvated antagonist resulting from the partial charge of another antagonist atom j.

The calculations were performed by using DelPhi, solving the Poisson−Boltzmann equation (Poisson−Boltzmann free energy − PBFE) in a linear approximation.[81−84] The electrostatic potentials were obtained using a focusing protocol, where the system filled 20, 30, 50, and 90% of the box stepwise, allowing for gradual refinement of boundary conditions. The inner dielectric constant in the calculations was $\epsilon = 2$, $\epsilon = 4$, and $\epsilon = 10$ for the protein and $\epsilon = 80$ for water. In the analysis, we compared the free energy change upon binding (ΔG_{bind}) of the two complexes obtained from a structure best representing the average within the last 2 ns of the MDS trajectory and also from that of the structures determined by X-ray crystallography (where missing residues were built in the structure and energy-minimized, keeping all other atoms frozen).

Acknowledgment. Financial support is acknowledged from a grant of the Hungarian Ministry of Health ETT 512/2006 (J.F.), and grant 9988-06 from NSERC (M.L.), as well as a

Ph.D. fellowship from the Richter Gedeon Rt. Centenáriumi Alapítvány (J.F., I.K.) and of the Bolyai Fellowship of the Hungarian Academy of Sciences (D.K.M.).

References

(1) Cheung, W. Y. Calmodulin: An overview. *FED Proc.* **1982**, *41*, 2253–2227.
(2) Kortvely, E.; Gulya, K. Calmodulin and various ways to regulate its activity. *Life Sci.* **2004**, *74*, 1065–1070.
(3) Vetter, S. W.; Leclerc, E. Novel aspects of calmodulin target recognition and activation. *Eur. J. Biochem.* **2003**, *270*, 404–414.
(4) Crivici, A.; Ikura, M. Molecular and structural basis of target recognition by calmodulin. *Annu. Rev. Biophys. Biomol. Struct.* **1995**, *24*, 85–116.
(5) Brokx, R. D.; Lopez, M. M.; Vogel, H. J.; Makhatadze, G. I. Energetics of target peptide binding by calmodulin reveals different modes of binding. *J. Biol. Chem.* **2001**, *276*, 14083–14091.
(6) Maler, L.; Blankenship, J.; Rance, M.; Chazin, W. J. Site−site communication in the EF-hand Ca^{2+}-binding protein calbindin D-9k. *Nat. Struct. Biol.* **2000**, *7*, 245–250.
(7) Vigil, D.; Gallagher, S. C.; Trewhella, J.; Garcia, A. E. Functional dynamics of the hydrophobic cleft in the N-domain of calmodulin. *Biophys. J.* **2001**, *80*, 2082–2092.
(8) Rao, S. T.; Wu, S.; Satyshur, K. A.; Ling, K. Y.; Kung, C.; et al. Structure of *Paramecium tetraurelia* calmodulin at 1.8 A resolution. *Protein Sci.* **1993**, *2*, 436–447.
(9) Chattopadhyaya, R.; Meador, W. E.; Means, A. R.; Quiocho, F. A. Calmodulin structure refined at 1.7 Å resolution. *J. Mol. Biol.* **1992**, *228*, 1177–1192.
(10) Heidorn, D. B.; Trewhella, J. Comparison of the crystal and solution structures of calmodulin and troponin C. *Biochemistry* **1988**, *27*, 909–915.
(11) Barbato, G.; Ikura, M.; Key, L. E.; Pastor, R. W.; Bax, A. Backbone dynamics of calmodulin studied by 15N relaxation using inverse detected two-dimensional NMR spectroscopy: The central helix is flexible. *Biochemistry* **1992**, *31*, 5269–5278.
(12) Wriggers, W.; Mehler, E.; Pitici, F.; Weinstein, H.; Schulten, K. Structure and dynamics of calmodulin in solution. *Biophys. J.* **1998**, *74*, 1622–1639.
(13) Yang, C.; Jas, G. S.; Kuczera, K. Structure and dynamics of calcium-activated calmodulin in solution. *J. Biomol. Struct. Dyn.* **2001**, *80*, 2082–2092.
(14) Shepherd, C. M.; Vogel, H. J. A molecular dynamics study of $Ca2^{+}$ -calmodulin: Evidence of interdomain coupling and structural collapse on the nanosecond timescale. *Biophys. J.* **2004**, *87*, 780–791.
(15) Fiorin, G.; Biekofshy, R. R.; Pastore, A.; Carloni, P. Unwinding the helical linker of calcium-loaded calmodulin: A molecular dynamics study. *Proteins: Struct., Funct., Genet.* **2005**, *61*, 829–839.
(16) Bayley, P. M.; Findlay, W. A.; Martin, S. R. Target recognition by calmodulin: Dissecting the kinetics and affinity of interactin using short peptide sequences. *Protein Sci.* **1996**, *5*, 1215–1228.
(17) Myre, M. A.; O'Day, D. H. Calmodulin binds to and inhibits the activity of phosphoglycerate kinase. *Biochim. Biophys. Acta* **2004**, *1693*, 177–183.
(18) Baehler, M.; Rhoads, A. Callmodulin signaling via the IQ motif. *FEBS Lett.* **2002**, *513*, 107–113.
(19) Rhoads, A. R.; Friedberg, F. Sequence motifs for calmodulin recognition. *FASEB J.* **1997**, *11*, 331–340.
(20) Meador, W. E.; Means, A. R.; Quiocho, F. A. Target enzyme recognition by calmodulin: 2.4 Å structure of a calmodulin−peptide complex. *Science* **1992**, *257*, 1251–1255.
(21) Tanaka, T.; Hidaka, H. Hydrophobic region function in calmodulin−enzyme interactions. *J. Biol. Chem.* **1980**, *255*, 11078–11080.
(22) Yang, C.; Kuczera, K. Molecular dynamics simulations of a calmodulin−peptide complex in solution. *J. Biomol. Struct. Dyn.* **2002**, *20*, 179–197.
(23) Roufogalis, B. D.; Minocherhomjee, A.-E.-V. M.; Al-Jobore, A. Pharmacological antagonism of calmodulin. *Can. J. Biochem. Cell Biol.* **1982**, *61*, 927–933.
(24) Hardcastle, I. R.; Rowlands, M. G.; Grimshaw, R. M.; Houghton, J.; Jarman, M.; et al. Homologs of idoxifene: Variation of estrogen receptor binding and calmodulin antagonism with chain length. *J. Med. Chem.* **1996**, *39*, 999–1004.
(25) Vertessy, B. G.; Harmat, V.; Boecskei, Z.; Naray-Szabo, G.; Orosz, F. Simultaneous binding of drugs with different chemical structures to $Ca2^{+}$ -calmodulin: Crystallographic and spectroscopic studies. *Biochemistry* **1998**, *37*, 15300–15310.
(26) Harmat, V.; Boecskei, Z.; Naray-Szabo, G.; Bata, I.; Csutor, S. A. A new potent calmodulin antagonist with arylalkylamine structure: Crystallographic, spectroscopic and functional studies. *J. Mol. Biol.* **2000**, *297*, 747–755.
(27) Jackson, A. E.; Puett, D. Binding of trifluoperazine and fluorene-containing compounds to calmodulin and adducts. *Biochem. Pharmacol.* **1986**, *35*, 4395–4400.
(28) Massom, L.; Lee, H.; Jarrett, H. W. Trifluoperazine binding to porcine brain calmodulin and skeletal muscle troponin C. *Biochemistry* **1990**, *29*, 671–681.
(29) Massom, L. R.; Lukas, T. J.; Persechini, A.; Kretsinger, R. H.; Watterson, D. M.; et al. Trifluoperazine binding to mutant calmodulins. *Biochemistry* **1991**, *30*, 663–667.
(30) Tanokura, M.; Yamada, K. Effects of trifluoperazine on calcium binding by calmodulin. A microcalorimetric study. *J. Biol. Chem.* **1985**, *260*, 8680–8682.
(31) Levin, R. M.; Weiis, B. Binding of trifluoperazine to the calcium-dependent activator of cyclic nucleotide phosphodiesterase. *Mol. Pharmacol.* **1977**, *13*, 690–697.
(32) Cook, W. J.; Walter, L. J.; Walter, M. R. Drug binding by calmodulin: Crystal structure of calmodulin−trifluoperazine complex. *Biochemistry* **1994**, *33*, 15259–15265.
(33) Vandonselaar, M.; Hickie, R. A.; Quail, J. W.; Delbaere, L. T. Trifluorperazine-induced conformational change in ($Ca2^{+}$) calmodulin. *Nat. Struct. Biol.* **1994**, *1*, 795.
(34) Yamaotsu, N.; Suga, M.; Hirono, S. Molecular dynamics simulation of the calmodulin-trifluoperazine complex in aqueous solution. *Biopolymers* **2001**, *58*, 410–421.
(35) Rizzon, R. C.; Toba, S.; Kuntz, I. D. Molecular basis for the Selectivity of Thiadiazole Urea Inhibitors with Stromelysin-1 and Gelatinase-A from Generalized Born Molecular Dynamics Simulations. *J. Med. Chem.* **2004**, *47*, 3065–3074.
(36) Andre, I.; Kesvatera, T.; Jonsson, B.; Akerfeld, K. S.; Linse, S. The role of electrostatic interactions in calmodulin−peptide complex formation. *Biophys. J.* **2004**, *87*, 1929–1938.
(37) Froloff, N.; Windemuth, A.; Honig, B. On the calculation of binding free energies using continuum methods: Application to MHC class I protein−peptide interactions. *Protein Sci.* **1997**, *6*, 1293–1301.
(38) Ladbury, J., E.; Williams, M. A. The extended interface: Measuring nonlocal effects in biomolecular interactions. *Curr. Opin. Struct. Biol.* **2004**, *14*, 562–569.
(39) Gabdoulline, R. R.; Wade, R. C. Biomolecular diffusional association. *Curr. Opin. Struct. Biol.* **2002**, *12*, 204–213.
(40) Karplus, M.; Kuriyan, J. Molecular dynamics and protein function. *Proc. Natl. Acad. Sci. U.S.A.* **2005**, *102*, 6679–6685.
(41) Mitra, A.; Sept, D. Binding and interaction of dinitroanilines with apicomplexan and kinetoplastid -tubulin. *J. Med. Chem.* **2006**, *49*, 5226–5231.
(42) Ivanov, A. A.; Baskin, I. I.; Palyulin, V. A.; Piccagli, L.; Baraldi, P. G.; et al. Molecular modeling and molecular dynamics simulation of the human A2B adenosine receptor. The study of the possible binding modes of the A2B receptor antagonists. *J. Med. Chem.* **2005**, *48*, 6813–6820.
(43) Schiott, B. Possible involvement of collective domain movement int he catalytic reaction of soluble epoxide hydrolase. *Int. J. Quantum Chem.* **2004**, *99*, 61–69.
(44) Archontis, G.; Simonson, T.; Karplus, M. Binding free energy components from molecular dynamics and Poisson−Boltzmann calculations. Application to amino acid recognition by aspartyl-tRNA synthetase. *J. Mol. Biol.* **2001**, *306*, 307–327.
(45) Meador, W. E.; Means, A. R.; Quiocho, F. A. Target enzyme recognition by calmodulin: 2.4 Å structure of a calmodulin−peptide complex. *Science* **1992**, *257*, 1251–1255.
(46) Drum, C. L.; Yan, S. Z.; Bard, J.; Shen, Y. Q.; Lu, D. Structural basis for the activation of anthrax adenylyl cyclase exotoxin by calmodulin. *Nature* **2002**, *415*, 396–402.
(47) Shen, Y. Q.; Lee, Y. S.; Soelaiman, S.; Bergson, P.; Lu, D.; et al. Physiological calcium concentrations regulate calmodulin binding and catalysis of adenylyl cyclase exotoxins. *EMBO J.* **2002**, *21*, 6721–6732.
(48) Osawa, M.; Swindells, M. B.; Tanikawa, J.; Tanaka, T.; Mase, T.; et al. Solution structure of calmodulin−W-7 complex: The basis of diversity in molecular recognition. *J. Mol. Biol.* **1998**, *276*, 165–176.
(49) Clapperton, J. A.; Martin, S. R.; Smerdon, S. J.; Gamblin, S. J.; Bayley, P. M. Structure of the complex of calmodulin with the target sequence of calmodulin-dependent protein kinase I: Studies of the kinase activation mechanism. *Biochemistry* **2002**, *41*, 14669–14679.
(50) Yap, K. L.; Yuan, T.; Mal, T. K.; Vogel, H. J.; Ikura, M. Structural basis for simultaneous binding of two carboxy-terminal peptides of plant glutamate decarboxyloase to calmodulin. *J. Mol. Biol.* **2003**, *328*, 193–204.
(51) Weigand, S.; Shuvalova, L.; Lukas, T. J.; Mirzoeva, S.; Watterson, D. M.; Anderson, W. F. High resolution structure of a calmodulin Rs20 peptide complex; To be published.
(52) Guo, Q.; Shen, Y.; Zhukovskaya, N. L.; Florian, J.; Tang, W. J. Structural and kinetic analyses of the interaction of anthrax adenylyl cyclase toxin with reaction products cAMP and pyrophosphate. *J. Biol. Chem.* **2004**, *279*, 29427–29435.

(53) Contessa, G. M.; Orsale, M.; Melino, S.; Torre, V.; Paci, M.; Desideri, A.; Cicero, D. O. Structure of calmodulin complexed with an olfactory CNG channel fragment and role of the central linker: Residual dipolar couplings to evaluate calmodulin binding modes outside the kinase family. *J. Biomol. NMR* **2005**, *31*, 185–199.
(54) Horvath, I.; Harmat, V.; Perczel, A.; Palfi, V.; Nyitrai, L.; Nagy, A.; Hlavanda, E.; Naray-Szabo, G.; Ovadi, J. The structure of the complex of calmodulin with KAR-2: A novel mode of binding explains the unique pharmacology of the drug. *J. Biol. Chem.* **2005**, *280*, 8266–8274.
(55) Kursula, P.; Vahokoski, J.; Wilmanns, M. Recognition of human death-associated protein kinases by calmodulin;To be published.
(56) Ikura, M.; Clore, G. M.; Gronenborn, A. M.; Zhu, G.; Klee, C. B.; Bax, A. Solution structure of a calmodulin-target peptide complex by multidimensional NMR. *Science* **1992**, *256*, 632–638.
(57) Maximciuc, A. A.; Putkey, J. A.; Shamoo, Y.; Mackenzie, K. R. Complex of calmodulin with a ryanodine receptor target reveals a novel, flexible binding mode. *Structure* **2006**, *14*, 1547–1556.
(58) Simonovic, M.; Zhang, Z.; Cianci, C. D.; Steitz, T. A.; Morrow, J. S. Structure of calmodulin alphaII-spectrin provides insight into regulation of cell plasticity;To be published.
(59) Brooks, B. R.; Bruccoleri, R. E.; Olafson, B. D.; States, D. J.; Swaminathan, S.; et al. CHARMM: A program for macromolecular energy, minimization and dynamics calculations. *J. Comput. Chem.* **1983**, *4*, 187–217.
(60) Jorgensen, W. L.; Chandrasekhar, J.; Madura, J. D.; Impey, R. W.; Klein, M. L. Comparison of simple potential functions for simulating liquid water. *J. Chem. Phys.* **1983**, *79*, 187–217.
(61) Nelson, M.; Humphrey, W.; Gursoy, A.; Dalke, A.; Kale, L., et al. NAMD—A parallel, object oriented molecular dynamics programs. *Int. J. Supercomput. Appl. High Perform. Comput.* **1996**, *10*, 251–268.
(62) Foloppe, N.; MacKerell, J. A. D. All-atom empirical force field for nucleic acids: Parameter optimization based on small molecule and condensed phase macromolecular target data. *J. Comput. Chem.* **2000**, *21*, 86–104.
(63) Yin, D.; MacKerell, J. A. D. Combined ab initio/empirical approach for the optimization of Lennard−Jones parameters. *J. Comput. Chem.* **1998**, *19*, 334–348.
(64) Kendall, R. A.; Apra, E.; Bernholdt, D. E.; Bylaska, E. J.; Dupuis, M., et al. High performance computational chemistry: An overview of NWChem a distributed parallel application. *Comput. Phys. Commun.* **2000**, *128*, 260–283.
(65) Apra, E.; Windus, T. L.; Straatsma, T. P.; Bylaska, E. J.; de Jong, W. *NWChem*, 4.7 ed.; Pacific Northwest National Laboratory: Richland, WA.
(66) Hohenberg, P.; Kohn, W. Inhomogeneous electron gas. *Phys. Rev.* **1964**, *136*, B864−B887.
(67) Sham, L. J. Self-consistent equations including exchange and correlation effects. *Phys. Rev.* **1965**, *140*, A1133−A1138.
(68) Kohn, W.; Becke, A. D.; Parr, R. G. Density functional theory of electronic structure. *J. Phys. Chem.* **1996**, *100*, 12974–12980.
(69) Becke, A. D. Density-functional thermochemistry. III. The role of exact exchange. *J. Chem. Phys.* **1993**, *98*, 5648–5652.
(70) Stevens, W. J.; Basch, H.; Krauss, M. Compact effective potentials and efficient shared-exponent basis sets for the first- and second-row atoms. *J. Chem. Phys.* **1984**, *81*, 6026–6033.
(71) Breneman, C. M.; Wiberg, K. B. Determining atom-centered monopoles from molecular electrostatic potentials. The need for high sampling density in formamide conformational analysis. *J. Comput. Chem.* **2004**, *11*, 361–373.
(72) Vaiana, A. C.; Cournia, Z.; Costescu, I. B.; Smith, J. C. AFMM: A molecular mechanics force field vibrational parametrization program. *Comput. Phys. Commun.* **2005**, *167*, 34–42.
(73) Grubmuller, H. *SOLVATE*, 1.0 ed.; Ludwig-Maximilians Universität, München; Theoretical Biophysics Group, Institute for Medical Optics: München.
(74) Ryckaert, J.-P.; Ciccotti, G.; Berendsen, H. J. C. Numerical integration of the Cartesian equations of motion for a system with constraints: molecular dynamics of n-alkanes. *J. Comp. Phys.* **1977**, *23*, 327–341.
(75) Essmann, U.; Perera, L.; Berkowitz, M. L.; Darden, T.; Lee, H., et al. A smooth particle mesh Ewald method. *J. Chem. Phys.* **1995**, *1995*, 8577–8593.
(76) Laberge, M. K. I.; Yonetani, T.; Fidy, J. R-state hemoglobin bound to heterotropic effectors: models of the DPG, IHP, and RSR13 binding sites. *FEBS Lett.* **2005**, *579*, 627–632.
(77) Feller, S. E.; Zhang, Y.; Pastor, R. W.; Brooks, B. R. Constant pressure molecular dynamics simulation: The Langevin piston method. *J. Chem. Phys.* **1995**, *103*, 4613–4621.
(78) McDonald, I. K.; Thornton, J. M. Satisfying hydrogen bonding potential in proteins. *J. Mol. Biol.* **1994**, *238*, 777–793.
(79) Karplus, M.; McCammon, J. A. Dynamics of proteins: elements and function. *Annu. Rev. Biochem.* **1983**, *52*, 263–300.
(80) Meinhold, L.; Smith, J. C. Fluctuations and correlations in crystalline protein dynamics: A simulation analysis of staphylococcal nuclease. *Biophys. J.* **2005**, *88*, 2554–2563.
(81) Rocchia, W.; Alexov, E.; Honig, B. Extending the applicability of the nonlinear Poisson−Boltzmann equation: Multiple dielectric constants and multivalent ions. *J. Phys. Chem. B.* **2001**, *105*, 6507–6514.
(82) Rocchia, W.; Sridharan, S.; Nicholls, A.; Alexov, E.; Chiabrera, A.; Honig, B. Rapid grid-based construction of the molecular surface for both molecules and geometric objects: application to the finite difference Poisson−Boltzmann method. *J. Comput. Chem.* **2002**, *23*, 128–137.
(83) Gilson, M.; Honig, B. Calculations of electrostatic potentials in an enzyme active site. *Nature* **1987**, *330*, 84–86.
(84) Nicholls, A.; Honig, B. A rapid finite difference algorithm, utilizing successive over-relaxation to solve the Poisson−Boltzmann equation. *J. Comput. Chem.* **1991**, *12*, 435–445.

JM701406E